



Cite this: *J. Mater. Chem. A*, 2020, **8**, 4308

Unravelling the selective growth mechanism of AlO_x with dimethylaluminum isopropoxide as a precursor in atomic layer deposition: a combined theoretical and experimental study†

Jiaqiang Yang,^a Kun Cao,^b Quan Hu,^a Yanwei Wen,^a Xiao Liu,^a Rong Chen^{a,b} and Bin Shan^{a*}

The selective encapsulation of noble metal catalysts is a newly developed method to maintain their durability and reactivity. In our work, we have found that AlO_x can preferentially encapsulate Pt nanoparticle facets with dimethylaluminum isopropoxide (DMAI) as an ALD precursor. The selectivity originates from the preferential DMAI decomposition mechanism on double hydroxyl sites of the Pt (111) facet, with the subsequent H_2O half cycle rapidly removing residual surface intermediates and regenerating the hydroxyls as reaction sites for subsequent cycles. Related microkinetic and experimental results confirm that by the substitution of one methyl in trimethylaluminum (TMA) with an isopropanol radical, DMAI as the precursor can preferentially coat the Pt (111) facets and leave other sites intact through controlling the ALD deposition parameters. The substituent effect in DMAI is also discussed in detail to give guidance to ALD precursor design. Combining theoretical and experimental studies, our work provides for the first time a feasible strategy to achieve selective decoration of AlO_x on Pt nanoparticles via ALD.

Received 21st October 2019
Accepted 28th January 2020

DOI: 10.1039/c9ta11575g

rsc.li/materials-a

1 Introduction

Pt catalysts have extensive applications in energy conversion and environmental purification due to their excellent catalytic performance in the oxygen reduction reaction as well as diesel exhaust and VOC elimination.^{1–7} However, the formation of larger Pt nanoparticles (NPs) when operated at high temperatures causes loss of the active surface area and sites of the catalyst.^{8–11} Chemical anchoring by strong metal–support interfacial interactions and physical barriers *via* oxide overcoating are utilized to maintain the stability of Pt nanoparticles under harsh conditions.^{9,12,13} Notably, atomic layer deposition (ALD) is considered an effective physical encapsulating strategy due to its precise control of thickness on the atomic scale. It has been reported that coating porous layers of Al_2O_3 , ZnO , ZrO_2 and CeO_2 on metal NPs *via* ALD can be used to stabilize the NPs and to hinder diffusion and agglomeration.^{14–18} The elaborately constructed composite structure demonstrates outstanding

resistance towards sintering in comparison to its bare counterpart upon thermal aging. However, uniform porous protective layers block surface sites and suppress the access of reactants to the active components, which causes loss of reactivity and increased light-off temperature.^{19,20}

To address this issue, the selective encapsulation method has been proposed by controllably depositing oxides at desired sites of Pt NPs *via* ALD. It is found that the reactive 3d-transition metal oxides are quite effective decorations for low-coordinated Pt sites. For example, Qin *et al.* revealed that low-coordinated Pt sites can be precisely blocked by Fe oxides *via* ALD; this generates Pt– FeO_x interfacial perimeter sites and enhances the selectivity of selective hydrogenation of cinnamaldehyde.²¹ Furthermore, combining theoretical and experimental studies, our group proposed edge-selective growth mechanisms with cyclopentadienyl precursors (MCp_2 , $\text{M} = \text{Fe}, \text{Co}, \text{and Ni}$); this method exhibits robust preferential growth on edge sites due to a more favorable splitting path of the precursors.¹¹ It is plausible that the site preference can be ascribed to low coordination numbers of the edge sites; in turn, preferential terrace encapsulation appears to be more difficult. Researchers have also devoted efforts to achieving preferential coating of terrace sites on Pt NPs. It was recently demonstrated that $\text{Ce}(\text{thd})_4$ as a Ce precursor enables the precise deposition of CeO_x on Pt (111) facets while leaving Pt (100) facets exposed.¹⁰ This fact again confirms the superiority of transition metal oxides for

^aState Key Laboratory of Material Processing and Die and Mould Technology, School of Materials Science and Engineering, Huazhong University of Science and Technology, Wuhan 430074, Hubei, China. E-mail: bshan@mail.hust.edu.cn

^bState Key Laboratory of Digital Manufacturing Equipment and Technology, School of Mechanical Science and Engineering, Huazhong University of Science and Technology, Wuhan 430074, Hubei, China. E-mail: rongchen@mail.hust.edu.cn

† Electronic supplementary information (ESI) available. See DOI: 10.1039/c9ta11575g

selective coating of Pt NPs. On the other hand, inert oxide encapsulation is equally important because it can passivate undesired sites to tailor the intrinsic selectivity and stability of catalysts for numerous reactions.^{8,19} Note that Al_2O_3 is one of the most used widely oxides for ALD inert encapsulation.^{22–24} Using the popular trimethylaluminum (TMA) as a precursor of Al_2O_3 , Peter C. Stair and co-workers found that Al_2O_3 merely preferentially nucleates at low-coordinated sites of Pd NPs and leaves the Pd (111) facets free.^{25,26} To our best knowledge, preferential decoration of inert Al_2O_3 on Pt facets has not been realized to date.²⁷ It is highly desirable to achieve selective Al_2O_3 growth on Pt terrace sites.

In this work, based on theoretical and experimental studies, we demonstrate that by using dimethylaluminum isopropoxide (DMAI) as the new Al_2O_3 precursor, we can achieve the preferential encapsulation of Pt (111). The DMAI adsorption and decomposition mechanisms on hydroxylated Pt (111), (100) and edge sites are proposed and compared. It is found that double hydroxyls at the facets are the primary active sites, and the existence of H_2O in the reaction can effectively remove residual intermediates at the Pt sites. Furthermore, our microkinetic analysis and experimental evidence show that AlO_x can preferentially encapsulate Pt (111) while keeping other facets exposed as potential reaction sites through properly tuning the ALD cycles. Furthermore, the substituent effects on DMAI are discussed. Our work opens a new avenue for tuning the properties of Pt nanoparticles *via* area-selective ALD for numerous chemical reactions.

2 Computational methods

2.1 Density functional theory calculation set

Density functional theory (DFT) calculations^{28,29} were performed with VASP code.^{30–32} The exchange and correlation energies are in the form of generalized gradient approximation (GGA), and the Perdew–Burke–Ernzerhof (PBE) and projector augmented wave (PAW) methods were used to depict the electron–ion interactions.³³ A cutoff energy of 400 eV and Monkhorst–Pack k-meshes of $3 \times 3 \times 1$ were set for the surface calculations. The structure was optimized until the Hellmann–Feynman force was smaller than $0.05 \text{ eV } \text{\AA}^{-1}$. The climbing-image nudged elastic band (CI-NEB) method was used to search the transition states of the elementary steps, with six intermediate images between the initial and final states. On the basis of our previous study,¹¹ we utilized the low-index facets (111) and (100) to imitate the terraces of Pt NPs, and the joints of the two facets were constructed as low-coordinated edge sites, as shown in Fig. 1a. $4 \times 4 \times 1$ supercells with five atomic layers were necessary for the low-index (111) and (100) facets in view of the long fragments of DMAI. A $13.78 \text{ \AA} \times 14.06 \text{ \AA}$ rectangular cell with eight atomic layers was built for the edge configuration. These corresponding facet models are shown in Fig. S1.† The top three layers of these models were allowed to relax during structure optimizing and energy calculation. A vacuum layer of at least 15 \AA was appended to eliminate the image cell interactions along the direction perpendicular to the surface. Note that the coordination numbers of Pt atom on the edge, (100),

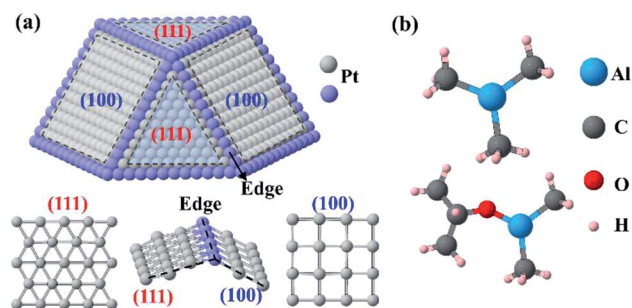


Fig. 1 The structures of (a) a typical Pt nanoparticle with Pt (111), Pt (100) and Pt edge sites and (b) the precursors trimethylaluminum (TMA) and dimethylaluminum isopropoxide (DMAI).

and (111) sites are 7, 8, and 9, respectively.¹¹ Comparative figures of the structures of the Al_2O_3 precursors (TMA and DMAI) are shown in Fig. 1b. One aluminum atom binds with three methyl groups and exhibits a planar configuration in TMA. Compared with TMA, the isopropanol radical ($\text{C}_2\text{H}_7\text{O}$) replaces one methyl in DMAI, which creates a larger fragment and asymmetric configuration. Structure differences between two precursors imply differences in their activity and selectivity. The adsorption energy ($E_{\text{ad}(X)}$) is defined as

$$E_{\text{ad}(X)} = E_{\text{slab}+X} - E_{\text{slab}} - E_X \quad (1)$$

where E_X and $E_{\text{slab}+X}$ correspond to the energies of the adsorbate itself and the surface with the adsorbate, respectively.

2.2 Experimental section

AlO_x deposition experiments were carried out with different reaction cycles on Pt nanoparticle facets *via* ALD. Note that the Pt nanoparticles were firstly supported on CeO_2 supports *via* the ALD method,³⁴ and all Pt/ CeO_2 samples in our work were prepared with two Pt ALD cycles. The particle sizes and distribution of the Pt nanoparticles at the CeO_2 nanospheres (NS) are shown in Fig. S2.† Uniform distribution of Pt nanoparticles at the CeO_2 nanospheres was found, and the average Pt particle size is about $2.30 \pm 0.36 \text{ nm}$. The ALD processes for the surface coating of the nanoparticles were performed in a homemade ALD reactor with a fluidized bed. When no precursor is introduced, the base pressure of the reactor is about 1.2 Torr. About 200 mg sample can be loaded into the designed powder holder, and the top and bottom are sealed by a stainless steel screen. Considering the poor volatility of DMAI at room temperature, the precursor DMAI is heated and maintained at 60°C during the deposition. In contrast, due to the good volatility of TMA, the stainless steel bubbler of TMA is maintained at room temperature. An integrated AlO_x cycle consists of 90 s pulse times of both H_2O and the AlO_x precursor (DMAI or TMA) and N_2 purge times of 120 s between the two precursors at the deposition temperature of 120°C . Different from the popular precursor of TMA in typical Al_2O_3 ALD, the nonpyrophoric DMAI precursor can avoid the hazards induced by the pyrophoric nature of TMA.^{35,36} The partial pressures of DMAI and H_2O are 40 and 30 Pa, respectively.

We combined high resolution transmission electron microscopy (HRTEM) with *in situ* diffuse reflectance infrared Fourier transform (*in situ* DRIFT) experiments to confirm the selective encapsulation on the Pt NPs. Regarding *in situ* DRIFT, CO adsorbed on different facets possesses different locations of adsorption peaks in the linear CO adsorption spectra; these peak areas indicate the amount of available sites for CO adsorption and also represent the amount of vacant surface sites after a certain number of AlO_x ALD cycles. *In situ* DRIFT was performed on a Thermo Scientific Nicolet iS50 spectrometer equipped with a MCT detector and a reaction cell (PIKE Technologies) fitted with a ZnSe window. The DRIFT spectra were recorded in the range of $650\text{--}4000\text{ cm}^{-1}$ with a resolution of 4 cm^{-1} and accumulation of 32 scans. All the samples were first pre-treated in an atmosphere of 20% O_2 balanced by N_2 at 300°C for 30 min to remove possible organic species in the ALD process; then, the temperature was cooled to 30°C . The background spectra were collected in a flow of 50 sccm of N_2 at 30°C . CO adsorption spectra were collected after treatment with 50 sccm of 1% CO. After the spectra were stable, a flow of 50 sccm of N_2 was used to remove physically adsorbed CO, and the CO chemical adsorption spectra could be obtained.

2.3 Microkinetic model of DMAI decomposition

A schematic of the Al_2O_3 ALD process is plotted in Fig. 2. It mainly involves two half cycles: the H_2O half cycle for surface hydroxylation and the Al-containing precursor half cycle for AlO_x formation. According to the initial chemical environment, we can divide the ALD process into two stages: nucleation and linear growth.¹¹ In the nucleation stage, only the hydroxyls exist at the surface, and DMAI binds with the hydroxyls and further decomposes. This process mainly occurs in the early stage of ALD. After that, the surface is saturated by the AlO_x species, where DMAI further adsorbs and decomposes to form the AlO_x thin film; this is generally referred to as the linear growth stage. In reality, the nucleation stage plays the crucial role in the intrinsic selective AlO_x growth at the Pt facets;¹¹ thus, we focus on the adsorption and decomposition of the precursor on different Pt facets in the nucleation stage in this work.

To quantitatively evaluate the deposition rates of AlO_x on different facets, a microkinetic model is essential to gain

insight into the DMAI adsorption and dissociation behaviors under relevant experimental conditions. In the model, the decomposition of DMAI mainly involves the adsorption and dissociative reaction processes. The rate constant (k_i) of the adsorption process was obtained by applying the collision theory³⁷ in eqn (2). Note that S as the sticking coefficient is assumed as unity for all adsorbed species. σ is the average area of an active site and was set as the areas of the models in our calculation. The other parameters are molecular mass (m_A), Boltzmann constant (k_B) and reaction temperature (T), respectively. Otherwise, the rate constants (k_i) of the surface reaction steps were obtained from transition state theory³⁸ as shown in eqn (3), and ΔE_i is a DFT-calculated surface reaction barrier. As we know, a normal microkinetic model of a catalytic reaction network requires that the reaction sites be recovered after an integrated reaction cycle because of the nature of the catalytic process.³⁹ However, in the deposition process of ALD, the available sites for precursor decomposition gradually reduce until all are covered by targeted AlO_x species as the process proceeds. Thus, we introduced a parameter to describe the amount of AlO_x species to simulate the realistic situation. The details are shown in Section 3.4.

$$k_i = \frac{S\sigma}{\sqrt{2\pi m_A k_B T}} \quad (2)$$

$$k_i = \frac{k_B T}{h} \exp\left(\frac{-\Delta E_i}{k_B T}\right) \quad (3)$$

3 Results and discussion

3.1 Hydroxylated sites on Pt facets

In the typical ALD process, the existence of H_2O precursor can hydroxylate the surface atoms to create favorable precursor adsorption and dissociation sites.^{25,40,41} Under realistic atmospheric conditions, H_2O dissociation is observed to form adsorbed hydroxyl species due to the presence of adsorbed atomic oxygen at the Pt slabs.^{42–44} Thus, hydroxylated Pt facets were chosen as the surface model for DMAI decomposition in our research. We give the variation of the relative energies about the distance of two hydroxyls to gain insight into the interactions between the hydroxyls in Fig. 3. At Pt (111), we can find that energy fluctuation under 0.1 eV occurs for hydroxyls with different distances, which demonstrates the weak interactions between the hydroxyls. It was also found that the top and bridge adsorption sites on Pt (111) have similar stability. Three different binding configurations, namely top-top (t-t), top-bridge (t-b) and bridge-bridge (b-b), as reasonable representations of hydroxyls binding on Pt (100) and edge facets, are shown in Fig. 3b and c. It was found that the stability of these structures follows the order $\text{b-b} > \text{t-b} > \text{t-t}$ due to the stronger bridge binding. Note that the nearest double hydroxyl binding is energetically unfavorable compared with the other b-b binding because of the shared Pt atoms. Except for this outlier, there is no appreciable change of binding strength with distance, indicating negligible interaction between hydroxyls.

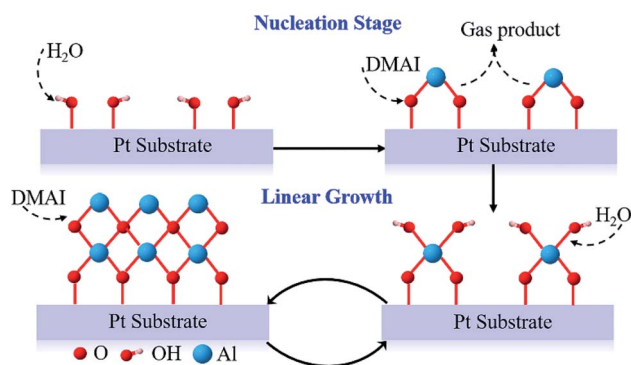


Fig. 2 Schematic of the reaction process of AlO_x ALD.

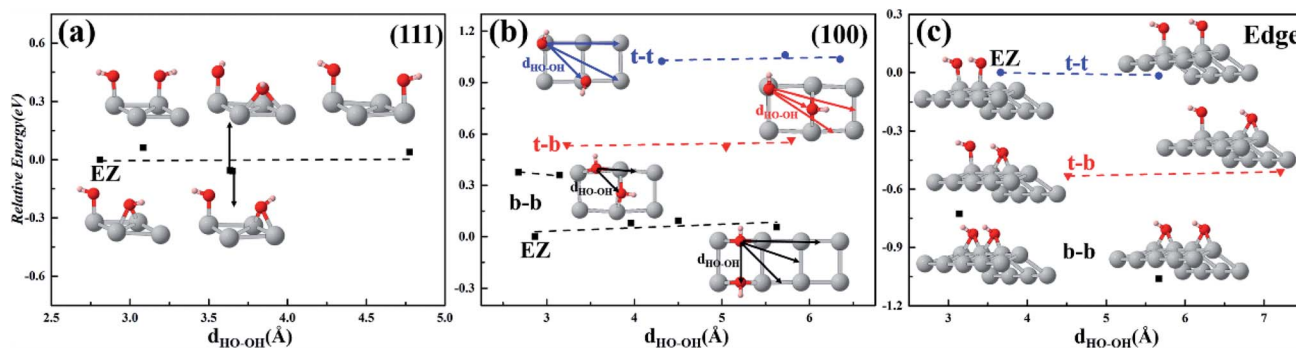
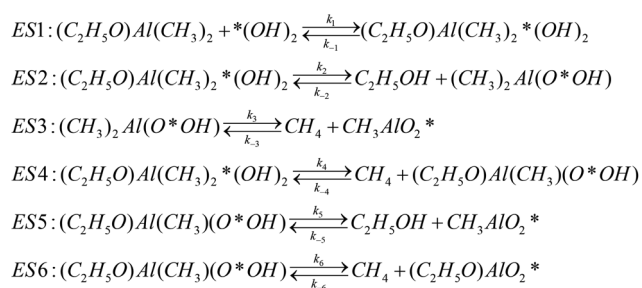


Fig. 3 The variation of the relative energies about the distance between two hydroxyls at (a) Pt (111), (b) Pt (100) and (c) Pt edge sites. Note that the relative energies were calculated with the energy of a certain structure as energy zero (EZ), and the distance ($d_{\text{HO-OH}}$) between double hydroxyls was defined as the distance between the oxygen atoms.

3.2 DMAI decomposition on Pt facets

Due to the existence of 4 and 6-coordinated Al atoms in bulk Al_2O_3 , we primarily considered the isolated and double hydroxyl models as the reaction sites. In addition, the surface model with more hydroxyl groups is unfavorable for the adsorption of planar Al precursors (DMAI and TMA). Considering that the neighboring distance of oxygen atoms is around 2.4–3.2 Å and the bond length of Al–O is about 1.7–2.1 Å in bulk Al_2O_3 , the double hydroxyls must be within a distance of 3.5–4.0 Å for effective binding with Al atoms in DMAI and TMA. A decomposition path of DMAI on Pt slabs with double hydroxyls is shown in Scheme 1 and Fig. 4. In this model, two hydroxyls on the slab capture one DMAI as the initial state of further reactions in elementary step 1 (ES1). Previous experimental work indicates that methane and isopropanol are the main products of DMAI decomposition *via* Al–C and Al–O scission, respectively;^{35,45–47} thus, two kinds of dissociation pathways may occur. One involves breaking the bonds between Al and O of isopropanol radical to form an isopropanol along ES2 and then produce a methane molecule after the breakage of the Al–C bond along ES3. Another pathway firstly produces a methane molecule *via* splitting of the Al–C bond in ES4 and subsequently releases an isopropanol and a methane molecule along ES5 and ES6, respectively. Apparently, two H atoms of hydroxyls can only assist the formation of two molecules, and the residual methyl or isopropanol radical is removed by the H_2O in the next ALD cycle. The corresponding energetics of DMAI decomposition on the Pt (111), (100) and edge sites are shown in Fig. 5.

Pt (111). Based on the discussion above, on the Pt (111) facet, our research focuses on the configuration of the two hydroxyls within the distance of 3.5 Å in Fig. 3a. Herein, we firstly chose the 1st configuration with the top and the most neighboring bridge binding as the initial state of DMAI adsorption. The reaction diagrams of DMAI dissociation are shown in Fig. 5a. We can see that a DMAI molecule binds with two hydroxyls *via* overcoming a low adsorption barrier of 0.18 eV, where the isopropanol radical locates atop the bridge-binding hydroxyls. The distance of 1.82 Å between H of the hydroxyl and O of the isopropanol radical and the angle between H of the hydroxyl and O of the isopropanol radical imply the existence of a hydrogen bond, which may be conducive to Al–O cleavage. Regarding the two different subsequent dissociation pathways, we can find that the formation of isopropanol *via* ES2 is easier than producing a methane in ES4 due to the lower barrier of Al–O bond breakage (0.28 eV) than of Al–C scission (0.64 eV). The two radicals of the residual intermediates are located on two sides of the Al atoms. Specifically, after releasing a methane molecule in ES4, migration of oxygen atoms bonded to the Pt slab leads to a structural reconstruction. The further dissociation of residual precursors along ES3, ES5 and ES6 were also studied, and the related structures of the intermediates are shown in Fig. S3.† A reaction barrier of 1.20 eV occurs for the production of $\text{CH}_3\text{AlO}_2^*$ in ES3, while a higher barrier of about 1.63 eV is needed for the same purpose in ES5. In ES6, methane formation possesses the same barrier as ES5. Herein, it is apparent that



Scheme 1 DMAI decomposition mechanism on Pt slabs with 2OH.

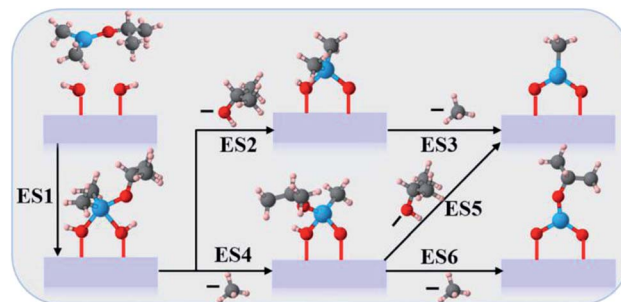


Fig. 4 Diagram of the elementary reaction steps of Scheme 1.

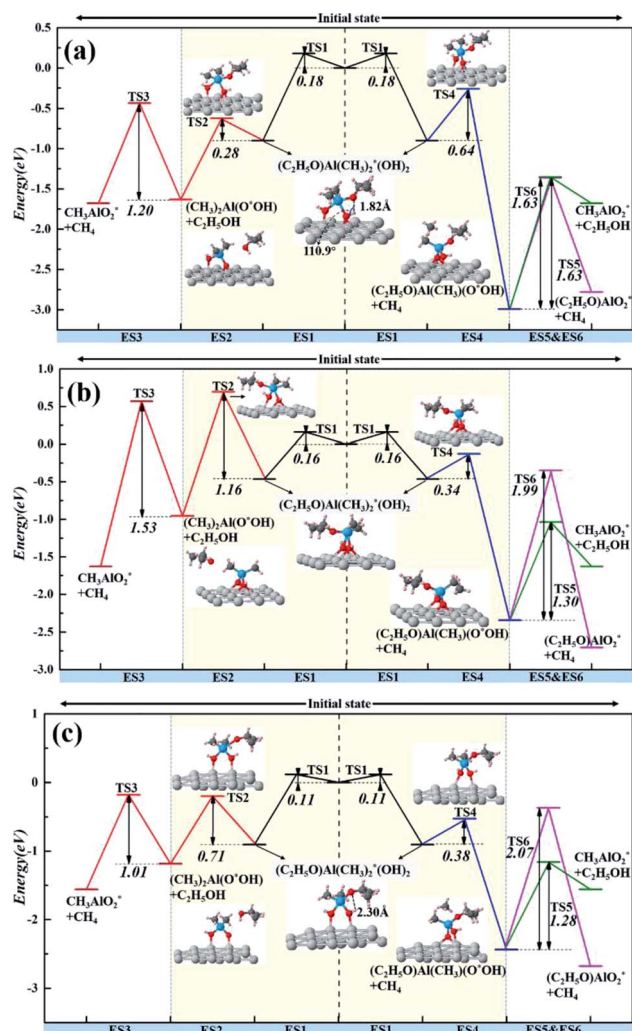


Fig. 5 The decomposition pathways of DMAI on Pt (a) (111), (b) (100) and (c) edge sites with double hydroxyls.

these second dissociation processes are more difficult due to higher barriers (≥ 1.20 eV) than the first dissociation of the precursor (< 0.65 eV). Moreover, we can find that the formation of reaction products in ES3, ES5 and ES6 is more endothermic compared with the first dissociations of DMAI along ES2 and ES4. Those results all illustrate that the second dissociation processes are unfavorable to proceed not only kinetically but also thermodynamically. Hence, decomposition of only one subgroup in DMAI is likely to occur on Pt (111).

On the other hand, the first-step decomposition of DMAI in the 2nd model with double top binding was also studied, as shown in Fig. S4.† Similar to the case discussed above, the formation of isopropanol has a low reaction barrier (0.29 eV) due to its similar adsorption configuration. Likewise, methane formation possesses a higher barrier (0.90 eV) than the isopropanol process. Generally speaking, Al–O scission is the predominant pathway for DMAI decomposition on Pt (111) facets.

Pt (100). On Pt (100), configurations with HO–OH distances of around 3.5 Å were selected as possible reaction sites for DMAI

adsorption and dissociation. Firstly, the energetic diagram of DMAI decomposition at the most stable b–b configuration is shown in Fig. 5b. In Fig. 5b, one DMAI molecule adsorbs at the hydroxyls with the energy barrier of 0.16 eV, where the methyl of DMAI is located on top of a hydroxyl and the other radicals are located on two sides of $\text{Al}^*(\text{OH})_2$. Then, the removal of a methyl in ES4 is easier than isopropanol formation because of the lower energy barrier of Al–C breakage. After releasing a methane or isopropanol, these configurations can be optimized as tetrahedral structures. Similarly, the subsequent dissociation processes of the residual precursors in ES3, ES5 and ES6 possess much higher energy barriers than the decomposition in ES2 and ES4, which suggests that DMAI dissociation would cease to proceed after ES2 or ES4. The structures of the related intermediates in the further decomposition processes are shown in Fig. S5.† We further considered another DMAI adsorption configuration, where the isopropanol radical is located atop one hydroxyl and the other methyl species are on the two sides of the $\text{Al}(\text{OH})_2$ radical, as shown in Fig. S6.† In the adsorption process, the H atom of one hydroxyl binds with the isopropanol; it exhibits a higher reaction barrier of about 0.87 eV, which indicates that it is more difficult for DMAI to bind with surface radicals through this structure. Furthermore, this adsorption configuration leads to energetically unfavorable isopropanol formation and slow methane formation.

Among other double hydroxyl configurations, b–b type with shared Pt atoms exhibits a high DMAI adsorption barrier of 0.73 eV due to Pt–O bond scission, and the t–b configuration shows high formation barriers of methane and isopropanol, as shown in Fig. S7.† In a word, the symmetric b–b hydroxyl groups in Fig. 5b show superior DMAI decomposition ability.

Pt edge. At the Pt edge sites, we compared the DMAI adsorption and decomposition behaviors at the t–t, t–b and b–b hydroxyl groups. We found that DMAI adsorption on the t–b type structure shows a higher adsorption barrier (0.61 eV) than that on t–t type (see Fig. S8a†) due to the change of the OH binding type from t–b to t–t type in the adsorption process. As for the b–b type structure, the DMAI decompositions all show much higher reaction barriers (> 1.0 eV) (see Fig. S8b†). Thus, we focused on DMAI adsorption and decomposition on the double hydroxyls with the t–t structure at the Pt edge sites. The corresponding energetic diagram is shown in Fig. 5c. It can be seen that DMAI binds with two top-binding hydroxyls by overcoming a barrier of 0.11 eV, and the isopropanol radical of DMAI locates atop one hydroxyl. Then, the H atom migrates to form an isopropanol molecule with a barrier of about 0.71 eV in ES2. The residual tetrahedral structure appears, and further dissociation exhibits a higher energy barrier of about 1.01 eV in ES3. On the other hand, compared with the decomposition along ES2, methane formation in ES4 is more favorable through a 0.38 eV barrier. After that, further dissociation along ES5 and ES6 is also more difficult in comparison with ES4. Structures of all the intermediates in the further decomposition processes are shown in Fig. S9.† It is concluded that the second dissociations along ES3, ES4 and ES5 also proceed with difficulty at the Pt edge sites.

Furthermore, the adsorption and decomposition of DMAI on the Pt facets with isolated hydroxyls were studied, as shown in

Fig. S10.† The reaction barriers of isopropanol and methane formation (denoted as $E_a(\text{Al}-\text{O})$ and $E_a(\text{Al}-\text{C})$, respectively) between the isolated and double hydroxyl models (denoted as Pt-1OH and Pt-2OH, respectively) are compared in Table 1. It was found that DMAI dissociation on Pt-2OH is not only more kinetically facile due to the lower decomposition barriers but is also more exothermic compared with Pt-1OH. In a word, double hydroxyl sites with suitable distance facilitate the decomposition of DMAI both thermodynamically and kinetically.

3.3 Hydrolyzation mechanism of residual precursors on Pt slabs

Due to the huge difficulty of further decomposition of residual intermediates after first-step dissociation on the Pt facets discussed above, we investigated the process where water in the H_2O half cycle decomposes the residual surface intermediates instead of direct dissociation. The process is referred to as the hydrolyzation mechanism, and corresponding reaction diagrams are shown in Fig. 6. On Pt (111), because Al-O bond scission is more kinetically facile than Al-C bond breakage (Fig. 5a), $(\text{CH}_3)_2\text{Al}(\text{O}^*\text{OH})$ is the primary residual surface intermediate after DMAI first-step decomposition. Accordingly, the hydrolyzation process of $(\text{CH}_3)_2\text{Al}(\text{O}^*\text{OH})$ at Pt (111) is considered in Fig. 6a. Obviously, the hydrolyzation in which $(\text{CH}_3)_2\text{Al}(\text{O}^*\text{OH})$ reacts with one gaseous H_2O is more favorable; it

shows a lower barrier of 0.16 eV than the direct decomposition (1.20 eV in Fig. 5a). Regarding the transition state (TS), we can see that O of H_2O gradually approaches the Al atoms, which can elongate the Al-C bond and promote breakage of the Al-C bond. Finally, an H atom of H_2O binds with the methyl of $(\text{CH}_3)_2\text{Al}(\text{O}^*\text{OH})$ to form gaseous methane, and the residual hydroxyl of H_2O binds with the Al atom to regenerate a new hydroxyl site for further Al_2O_3 growth. In contrast, Al-C scission in ES4 is more favorable than Al-O breakage at the Pt (100) facet, as shown in Fig. 5b, and we only consider the hydrolyzation of the production of ES4 ($(\text{C}_2\text{H}_5\text{O})\text{Al}(\text{CH}_3)(\text{O}^*\text{OH})$) in Fig. 6b. We found that the H atom firstly binds with O of the residual radical *via* hydrogen bonding in the transition state, which stretches the Al-O bond and favors its scission. After this, the hydroxyl of H_2O recombines with the Al-group and an isopropanol is released; this exhibits a lower barrier compared with the direct decomposition process in Fig. 5b. This situation also occurs on edge sites, as shown in Fig. 6c. The hydrogen of H_2O interacts with the oxygen of isopropanol *via* hydrogen bonding to assist decomposition of the residual intermediates, with a barrier of 0.19 eV. Meanwhile, it was also found that the hydrolyzation processes are more exothermic than the direct decomposition of the residual intermediates. Accordingly, H_2O as the critical assistant for further dissociation not only decreases the decomposition barrier in kinetics, but also makes the process spontaneous by thermodynamics. On the other hand, after the hydrolyzation, similar configurations of the single methyl appear at different Pt facets. A previous study of ALD with a TMA precursor indicated that the remaining single methyl binding Al can be easily removed by the production of CH_4 through water exposure.²⁷

Table 1 The formation barriers of isopropanol and methane ($E_a(\text{Al}-\text{O})$ and $E_a(\text{Al}-\text{C})$) on Pt facets with isolated and double hydroxyls (Pt-1OH and Pt-2OH)

	Pt-1OH		Pt-2OH	
	$E_a(\text{Al}-\text{O})$	$E_a(\text{Al}-\text{C})$	$E_a(\text{Al}-\text{O})$	$E_a(\text{Al}-\text{C})$
(111)	1.26	1.80	0.28	0.64
(100)	0.85	0.73	1.16	0.34
Edge	0.65	—	0.71	0.38

3.4 Microkinetic models of DMAI decomposition

Based on the discussion above, we established a simplified microkinetic model of DMAI decomposition on Pt facets with double hydroxyls as the reasonable AlO_x deposition model. In

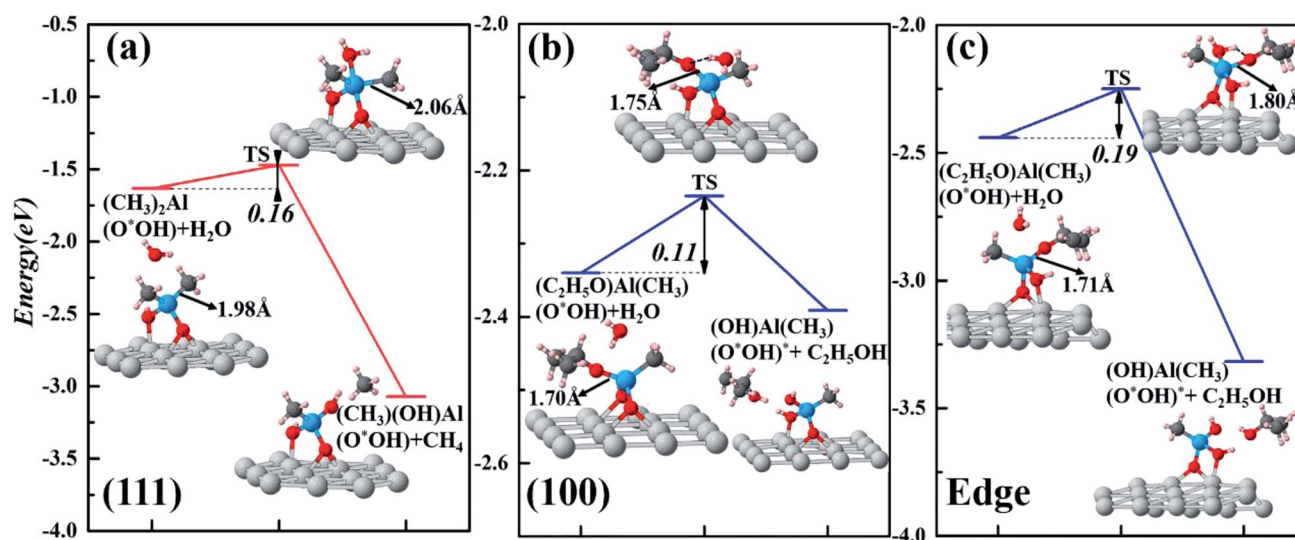


Fig. 6 The hydrolyzation pathways on different Pt sites: (a) Pt(111), (b) Pt(100) and (c) Pt edge sites.

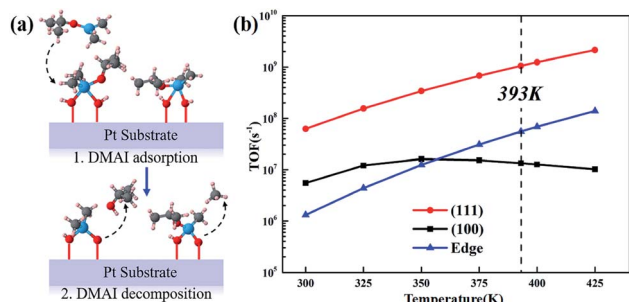


Fig. 7 (a) Schematic of DMAI decomposition; (b) AlO_x deposition rates on different Pt sites at 300–425 K.

the model, we only consider the DMAI adsorption and first-step decompositions (ES1, ES2 and ES4 in Scheme 1), as illustrated in Fig. 7a. Furthermore, the DMAI adsorption steps are assumed to be quasi-equilibrated ($r_1 = 0$) due to the relatively low adsorption barriers. Because the decomposition steps are dramatically exothermic, these steps are treated as irreversible processes. Based on this, the overall deposition rate (R) can be summarized as the sum of the forward rates ($r_2 + r_4$) of both DMAI decomposition steps (ES2 and ES4), as follows:

$$\begin{aligned} r_1 &= k_1 \theta^*(\text{OH})_2 P - k_{-1} \theta(\text{C}_2\text{H}_5\text{O})\text{Al}(\text{CH}_3)_2^*(\text{OH})_2 = 0 \\ r_2 &= k_2 \theta(\text{C}_2\text{H}_5\text{O})\text{Al}(\text{CH}_3)_2^*(\text{OH})_2 \\ r_4 &= k_4 \theta(\text{C}_2\text{H}_5\text{O})\text{Al}(\text{CH}_3)_2^*(\text{OH})_2 \\ R &= r_2 + r_4 \end{aligned}$$

where R , r_i and k_i are the overall reaction rate, rate of the elementary step i and rate constant of the elementary step i , respectively. P is the partial pressure of DMAI in the precursor flow and is set as 40 Pa.

A crucial assumption is that the amount of residual products after first-step decomposition is set as a constant ($1 - a$) to represent the coverage of deposited AlO_x at the Pt facets, based on the fact that these residual products can be facily transformed into AlO_x species through hydrolyzation processes. More importantly, this assumption can simulate the realistic surface situation where as the ALD cycles increase, AlO_x gradually covers the Pt slabs and causes changes in the amount of free sites available for DMAI adsorption and decomposition in the ALD process. On the basis of this consideration, we can obtain the overall deposition rate expression as follows:

$$\begin{aligned} \theta^*(\text{OH})_2 + \theta(\text{C}_2\text{H}_5\text{O})\text{Al}(\text{CH}_3)_2^*(\text{OH})_2 + \theta(\text{AlO}_x) &= 1 \\ \theta(\text{AlO}_x) &= 1 - a \\ \Rightarrow \theta^*(\text{OH})_2 + \theta(\text{C}_2\text{H}_5\text{O})\text{Al}(\text{CH}_3)_2^*(\text{OH})_2 &= a (0 \leq a \leq 1) \end{aligned}$$

$$R = \frac{a(k_2 + k_4)k_1 P}{k_{-1} + k_1 P}$$

From these formulas, we can find that the factor a , representing the available surface sites after a certain number of ALD cycles, only linearly affects the deposition rate. Thus, we assume a as 0.5 as the representative example of partially coated Pt facets. Furthermore, taking account of the larger barrier of the

reversible process than of the forward process in DMAI adsorption, the reversible reaction rate constant k_{-1} is far less than $k_1 P$ of the forward reaction. Thus, the overall reaction rate can be further simplified to:

$$R = 0.5(k_2 + k_4)$$

According to the microkinetic expression, we calculated the AlO_x deposition rates at different facets in the temperature range from 300 to 425 K, as shown in Fig. 7b. The dashed line denotes the experimental temperature (393 K). We can find that at 393 K, AlO_x deposition at Pt (111) is faster than at other slabs, which suggests a preference for AlO_x growth at Pt (111) with DMAI as the precursor. This trend was maintained in the temperature zone we studied due to the much higher deposition rate at Pt (111). Meanwhile, at 393 K, the rate difference between the edge sites and Pt (100) is relatively small in comparison with the deviations between Pt (111) and the other sites. Notably, the deposition rate at Pt (100) tends to a steady value above 350 K due to the relatively weak DMAI adsorption. The largest difference in the deposition rates at different slabs is smaller than 2 orders of magnitude, which also indicates that all the Pt sites will be covered by AlO_x species after enough ALD cycles and, therefore, the growth preference can no longer be maintained. In summary, site preference of Pt slabs can be achieved through tailoring the ALD cycles with DMAI as the Al-containing precursor.

Actually, a previous related experimental study indicates that the temperature window of AlO_x deposition with DMAI as a precursor is about 120–150 °C (393–423 K).^{35,46} In this temperature window, according to the theoretical results, relatively high temperature brings about simultaneous promotion of the reaction rates at the (111) and edge sites, which weakens the difference in the effects of the AlO_x deposition rate on the different sites and leads to less remarkable selectivity. On the other hand, at temperatures lower and higher than the realistic temperature window, the surface reaction process may be different from the standard ALD process. At temperatures below 100 °C (373 K), because the thermal energy is insufficient for a complete binary surface half reaction to occur, the growth rate is very low.³⁵ Furthermore, at low temperature, it is difficult to remove physically adsorbed DMAI in the N_2 purge process; also, there is unavoidable DMAI residue in the ALD chamber, which affects the next ALD process. At elevated temperatures of 180–210 °C (453–483 K), an additional CVD effect may occur through decomposition of the precursor due to high substrate temperatures.³⁵ These processes are not included in our theoretical model based on the experimental situation at the temperature of 120 °C (393 K). This also means that due to the changing reaction processes, it is relatively difficult to predict the reaction behaviour beyond this temperature window with this model.

3.5 Experimental evidence of selective AlO_x growth

Our experiment of Pt ALD with DMAI as a precursor also confirmed the selectivity of AlO_x deposition on Pt facets. FTIR signals of CO chemisorption on AlO_x -coated Pt nanoparticles with 0, 1, 3 and 5 ALD cycles are shown in Fig. 8. The three

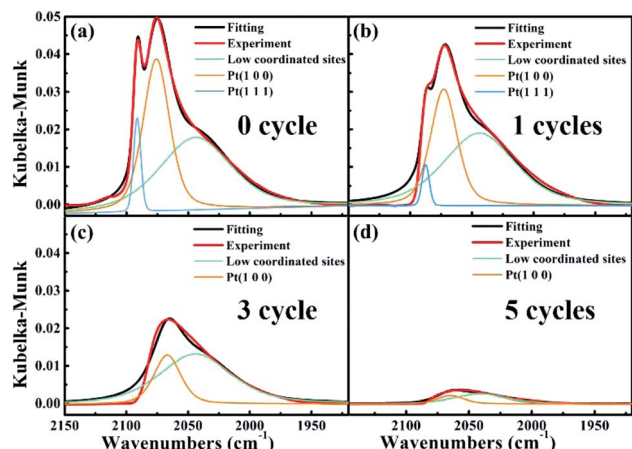


Fig. 8 Fitting curves of the linear CO adsorption spectra on AlO_x -coated Pt nanoparticles after (a) 0, (b) 1, (c) 3 and (d) 5 ALD cycles.

fitting peaks of the linear adsorption curves are assigned to CO adsorbed on the Pt (111) (blue), (100) (orange), and low-coordinated sites (green) according to previous work.^{26,48} Because the vertex site only occupies a small piece of the surface area of the nanoparticle, the low-coordinated sites are attributed to edge sites.⁴¹ It should be noted that the peak area in Fig. 8 represents the residual Pt sites after a certain number of ALD cycles. It was found that after 3 ALD cycles, the signal of the Pt (111) facets had already disappeared and the signals of Pt (100) and edge sites still existed, which demonstrates that Pt (111) is entirely covered by deposited AlO_x but that the Pt (100) and edge sites remain available for CO adsorption. Furthermore, the HRTEM image of AlO_x -coated Pt nanoparticles with 3 ALD cycles is shown in Fig. S11.† Because the amorphous AlO_x thin film shows ambiguous lattice fringes, we only accounted for the difference in material contrast; we found that the Pt NPs appear to be partially encapsulated, but detailed information about the coated facets was difficult to obtain. Combining HRTEM with the FTIR data, we can conclude that selective decoration of AlO_x on Pt (111) was achieved in the sample with 3 AlO_x ALD cycles. This experimental phenomenon agrees well with the theoretical predictions of the site preference of AlO_x growth. Another trend is that as the ALD cycles of AlO_x continue

to increase, the signals of the Pt facets gradually decrease to zero. This situation can be ascribed to the relatively small difference in the intrinsic deposition rates on Pt facets according to the microkinetic results in Fig. 7b. Generally speaking, our experimental results give credible evidence for selective AlO_x encapsulation at Pt (111) with the DMAI precursor.

According to previous studies on selective encapsulation,^{10,49} we expected that preferential coating on Pt (111) would be favourable for achieving superior thermal stability of Pt NPs. On the other hand, the nonreactive interface of inert AlO_x and the Pt NPs cannot provide new catalytic sites. Thus, the advantage of partial Al_2O_3 encapsulation on Pt NPs is achieving stability while sustaining the reactivity for as long as possible. Pt nanoparticles have extensive applications in energy fields in view of their high reactivity towards various chemical processes. Especially, the low-index (111), (100), and (110) facets of Pt have much lower activity than the high-index planes with high densities of atomic steps, ledges, and kinks as active sites for ORR, HOR, HER, *etc.*^{50–52} However, in a fuel cell environment, Pt particles suffer from Ostwald ripening and agglomeration, which leads to degradation of the Pt NPs and loss of the precious metal catalyst in fuel cell cathodes.⁵¹ Our work may provide a feasible strategy for preferential decoration of specific facets of Pt nanoparticles to balance reactivity and stability, which provides novel guidance for the design of fuel cell catalysts.

3.6 Substituent effects in DMAI precursor

The TMA decomposition pathways on Pt facets with double hydroxyls were studied and are shown in Fig. S12.† It was found that TMA decomposition proceeds more easily than DMAI decomposition; more importantly, the small barrier difference at different facets indicates no selectivity of ALD with TMA precursor, which agrees well with the experimental results shown in Fig. S13.† The behaviour of TMA at Pt nanoparticles was also demonstrated in a previous study.²⁷ Furthermore, to explain the selectivity difference of TMA and DMAI in nature, we considered the substituent effects on charge distribution and steric hindrance, as shown in Fig. 9. We found that because of the stronger electronegativity of oxygen than of carbon atom, more electrons of the aluminum atom in DMAI transfer to the

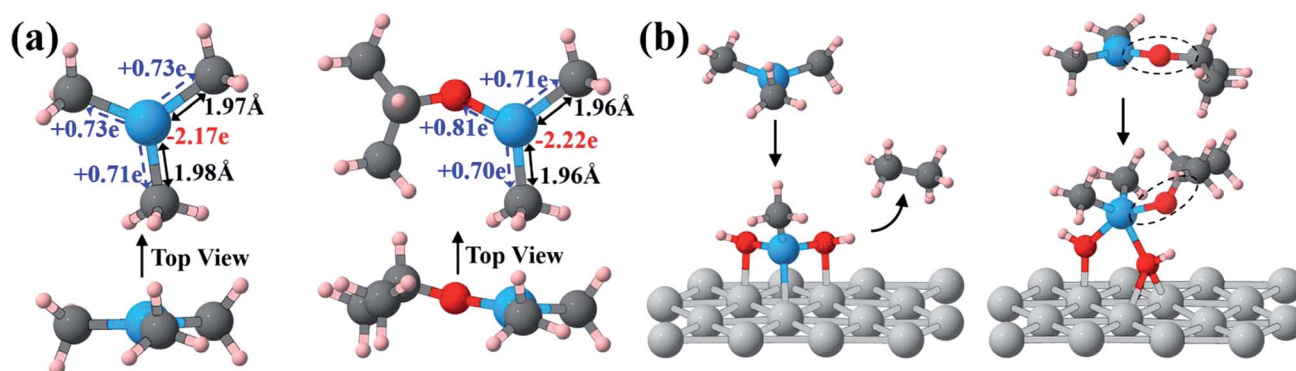


Fig. 9 (a) The charge transfer and Al–C bond lengths of TMA and DMAI and (b) structure changes before and after TMA and DMAI adsorption.

related binding atoms compared with that of TMA, which results in a more positive valence of Al atom in DMAI. This gives rise to stronger electrostatic interactions between the Al and C atoms of DMAI, which is manifested by the shorter Al–C bond lengths and more difficult Al–C scissions in DMAI compared with those in TMA. Also, the rigid structure of TMA consisting of three Al–CH₃ groups cannot release the repulsive interaction from the hydroxylated surface when TMA gradually approaches the adsorption sites. To some extent, this explains the barrierless decomposition of TMA to form C₂H₆ at the (111) and edge sites and the weak TMA adsorption as well as the facile TMA dissociation at (100) shown in Fig. S12.† In turn, the rotary Al–O–C bonds enable the isopropanol fragment to move far away from the surface through the slight spontaneous relaxation of the local structure, as shown in Fig. 9b; this results in stable DMAI adsorption. In a word, the isopropanol fragment of DMAI gives rise to a strong Al–C bond and stable surface adsorption. The substituent effect in DMAI enables selective deposition of AlO_x. Furthermore, the stable adsorption configuration of DMAI at Pt (111) provides favorable Al–O scission through hydrogen bond effects, which enables relatively high deposition activity at Pt (111) compared to the other sites.

4 Conclusions

In our work, we find that DMAI can be used as a precursor to selectively decorate Pt facets with inert AlO_x. Through our computations, we propose a mechanism of DMAI decomposition on hydroxylated Pt slabs and find that double hydroxyl sites at the Pt facets enable facile DMAI decomposition in comparison with the single hydroxyl model. Furthermore, hydrolyzation of residual surface intermediates is more favorable than their direct dissociation without H₂O participation. Further microkinetic analysis and experimental evidence indicates that AlO_x with DMAI as a precursor and Al-containing source can preferentially coat the Pt (111) surface and leave other sites available for catalytic reactions *via* tailoring the ALD cycles due to the relatively high intrinsic decomposition reactivity of DMAI at the Pt (111) facets. The substituent effect leads to strong Al–C bonding in DMAI and stable DMAI adsorption, which gives clear guidance for ALD precursor design. In general, our work affords new insight into the selective growth mechanism and provides a feasible strategy for selective decoration of Pt nanoparticles.

Conflicts of interest

There are no conflicts to declare.

Acknowledgements

The National Natural Science Foundation of China (Grants 51702106, 51871103, 51572097 and 51575217), Fundamental Research Funds for the Central Universities (2018KFYYXJJ031) and program for HUST Academic Frontier Youth Team (2018QYTD03) supported this work. Thanks to SCTS/CGCL HPCC of HUST for providing computing resources and

technical support. We thank Jie Zhang (Hubei University) and Chun Du (Huazhong University of Science and Technology) for the helpful discussions.

Notes and references

- 1 B. Lim, M. J. Jiang, P. H. C. Camargo, E. C. Cho, J. Tao, X. M. Lu, Y. M. Zhu and Y. N. Xia, *Science*, 2009, **324**, 1302–1305.
- 2 Y. Nie, L. Li and Z. D. Wei, *Chem. Soc. Rev.*, 2015, **44**, 2168–2201.
- 3 M. Kim, M. Bertram, M. Pollmann, A. Oertzen, A. S. Mikhailov, H. H. Rotermund and G. Ertl, *Science*, 2001, **292**, 1357–1360.
- 4 B. Qiao, A. Wang, X. Yang, L. F. Allard, Z. Jiang, Y. Cui, J. Liu, J. Li and T. Zhang, *Nat. Chem.*, 2011, **3**, 634–641.
- 5 S. Weon, J. Kim and W. Choi, *Appl. Catal., B*, 2018, **220**, 1–8.
- 6 J. J. Li, S. C. Cai, E. Q. Yu, B. Weng, X. Chen, J. Chen, H. P. Jia and Y. J. Xu, *Appl. Catal., B*, 2018, **233**, 260–271.
- 7 Z. Song, B. Wang, N. Cheng, L. Yang, D. Banham, R. Li, S. Ye and X. Sun, *J. Mater. Chem. A*, 2017, **5**, 9760–9767.
- 8 J. L. Lu, B. S. Fu, M. C. Kung, G. M. Xiao, J. W. Elam, H. H. Kung and P. C. Stair, *Science*, 2012, **335**, 1205–1208.
- 9 X. Liu, Q. Zhu, Y. Lang, K. Cao, S. Chu, B. Shan and R. Chen, *Angew. Chem., Int. Ed.*, 2017, **56**, 1648–1652.
- 10 K. Cao, L. Shi, M. Gong, J. Cai, X. Liu, S. Chu, Y. Lang, B. Shan and R. Chen, *Small*, 2017, **13**, 1700648.
- 11 Y. W. Wen, J. M. Cai, J. Zhang, J. Q. Yang, L. Shi, K. Cao, R. Chen and B. Shan, *Chem. Mater.*, 2019, **31**, 101–111.
- 12 X. Liu, Y. Tang, M. Shen, W. Li, S. Chu, B. Shan and R. Chen, *Chem. Sci.*, 2018, **9**, 2469–2473.
- 13 X. Liu, J. Yang, G. Shen, M. Shen, Y. Zhao, K. Cho, B. Shan and R. Chen, *Nanoscale*, 2019, **11**, 8150–8159.
- 14 H. Yi, H. Du, Y. Hu, H. Yan, H.-L. Jiang and J. Lu, *ACS Catal.*, 2015, **5**, 2735–2739.
- 15 J. Lu, B. Liu, J. P. Greeley, Z. X. Feng, J. A. Libera, Y. Lei, M. J. Bedzyk, P. C. Stair and J. W. Elam, *Chem. Mater.*, 2012, **24**, 2047–2055.
- 16 Y. Lei, S. Lee, K.-B. Low, C. L. Marshall and J. W. Elam, *ACS Catal.*, 2016, **6**, 3457–3460.
- 17 T. M. Onn, S. Zhang, L. Arr froyo-Ramirez, Y.-C. Chung, G. W. Graham, X. Pan and R. J. Gorte, *ACS Catal.*, 2015, **5**, 5696–5701.
- 18 L. Adijanto, D. A. Bennett, C. Chen, A. S. Yu, M. Cargnello, P. Fornasiero, R. J. Gorte and J. M. Vohs, *Nano Lett.*, 2013, **13**, 2252–2257.
- 19 X. H. Liang, J. H. Li, M. Yu, C. N. McMurray, J. L. Falconer and A. W. Weimer, *ACS Catal.*, 2011, **1**, 1162–1165.
- 20 Z. Shang and X. Liang, *Nano Lett.*, 2017, **17**, 104–109.
- 21 Q. Hu, S. Wang, Z. Gao, Y. Li, Q. Zhang, Q. Xiang and Y. Qin, *Appl. Catal., B*, 2017, **218**, 591–599.
- 22 L. Chen, J. G. Connell, A. Nie, Z. Huang, K. R. Zavadil, K. C. Klavetter, Y. Yuan, S. Sharifi-Asl, R. Shahbazian-Yassar, J. A. Libera, A. U. Mane and J. W. Elam, *J. Mater. Chem. A*, 2017, **5**, 12297–12309.
- 23 Z. Fan, Z. Xu, S. Yan and Z. Zou, *J. Mater. Chem. A*, 2017, **5**, 8402–8407.

- 24 H. Kou, X. Li, H. Shan, L. Fan, B. Yan and D. Li, *J. Mater. Chem. A*, 2017, **5**, 17881–17888.
- 25 H. Feng, J. Lu, P. C. Stair and J. W. Elam, *Catal. Lett.*, 2011, **141**, 512–517.
- 26 H. Zhang, X.-K. Gu, C. Canlas, A. J. Kropf, P. Aich, J. P. Greeley, J. W. Elam, R. J. Meyers, J. A. Dumesic, P. C. Stair and C. L. Marshall, *Angew. Chem., Int. Ed.*, 2014, **53**, 12132–12136.
- 27 J. Lu, B. Liu, N. P. Guisinger, P. C. Stair, J. P. Greeley and J. W. Elam, *Chem. Mater.*, 2014, **26**, 6752–6761.
- 28 P. Hohenberg and W. Kohn, *Phys. Rev.*, 1964, **136**, B864–B871.
- 29 W. Kohn and L. J. Sham, *Phys. Rev.*, 1965, **140**, A1133–A1138.
- 30 G. Kresse and J. Hafner, *Phys. Rev. B: Condens. Matter Mater. Phys.*, 1993, **47**, 558–561.
- 31 G. Kresse and J. Hafner, *Phys. Rev. B: Condens. Matter Mater. Phys.*, 1994, **49**, 14251–14269.
- 32 G. Kresse and J. Furthmüller, *Comput. Mater. Sci.*, 1996, **6**, 15–50.
- 33 G. Kresse and D. Joubert, *Phys. Rev. B: Condens. Matter Mater. Phys.*, 1999, **59**, 1758–1775.
- 34 Q. Hu, K. Cao, Y. Lang, R. Chen, S. Chu, L. Jia, J. Yue and B. Shan, *Catal. Sci. Technol.*, 2019, **9**, 2664–2672.
- 35 W. Cho, K. Sung, K. S. An, S. S. Lee, T.-M. Chung and Y. Kim, *J. Vac. Sci. Technol., A*, 2003, **21**, 1366–1370.
- 36 W. Ban, S. Kwon, J. Nam, J. Yang, S. Jang and D. Jung, *Thin Solid Films*, 2017, **641**, 47–52.
- 37 J. Yang, J. Zhang, X. Liu, X. Duan, Y. Wen, R. Chen and B. Shan, *J. Catal.*, 2018, **359**, 122–129.
- 38 K. Reuter and M. Scheffler, *Phys. Rev. B: Condens. Matter Mater. Phys.*, 2006, **73**, 045433.
- 39 J. Yang, L. Shi, X. Liu, Y. Wen, K. Cho, Y. Zhao, R. Chen and B. Shan, *J. Catal.*, 2019, **371**, 276–286.
- 40 J. W. Elam and S. M. George, *Chem. Mater.*, 2003, **15**, 1020–1028.
- 41 A. Mameli, B. Karasulu, M. A. Verheijen, B. Barcones, B. Macco, A. J. M. Mackus, W. M. M. E. Kessels and F. Roozeboom, *Chem. Mater.*, 2019, **31**, 1250–1257.
- 42 G. B. Fisher and B. A. Sexton, *Phys. Rev. Lett.*, 1980, **44**, 683.
- 43 M. Kiskinova, G. Pirug and H. P. Bonzel, *Surf. Sci.*, 1985, **150**, 319–338.
- 44 G. B. Fisher and J. L. Gland, *Surf. Sci.*, 1980, **94**, 446–455.
- 45 S. E. Potts, G. Dingemans, C. Lachaud and W. M. M. Kessels, *J. Vac. Sci. Technol., A*, 2012, **30**, 021505.
- 46 K. S. An, W. Cho, K. Sung, S. S. Lee and Y. Kim, *Bull. Korean Chem. Soc.*, 2003, **24**, 1659–1663.
- 47 J. Yang, B. S. Eller, M. Kaur and R. Nemanich, *J. Vac. Sci. Technol., A*, 2014, **32**, 021514.
- 48 F. Hoxha, B. Schimmoeller, Z. Cakl, A. Urakawa, T. Mallat, S. E. Pratsinis and A. Baiker, *J. Catal.*, 2010, **271**, 115–124.
- 49 J. Cai, J. Zhang, K. Cao, M. Gong, Y. Lang, X. Liu, Sh. Chu, B. Shan and R. Chen, *ACS Appl. Nano Mater.*, 2018, **1**, 522–530.
- 50 C. M. Zalitis, A. R. Kucernak, J. Sharman and E. Wright, *J. Mater. Chem. A*, 2017, **5**, 23328–23338.
- 51 S. Sui, X. Wang, X. Zhou, Y. Su, S. Riffat and C. Liu, *J. Mater. Chem. A*, 2017, **5**, 1808–1825.
- 52 A. Chen and P. Holt-Hindle, *Chem. Rev.*, 2010, **110**, 3767–3804.